PHY417S

November 2, 2016

Microwave Optics

Melissa Wu and Ji Won Park
Instructor: Professor Seog Oh

Abstract

We investigated the optical properties of microwaves in seven different experiments. We confirmed the laws of reflection and refraction, the equation for intensity transmission of light through a polarizer, and the diffractive behaviour of light as it passes through single and double slits. We used a Fabry-Perot interferometer to determine the wavelength of our microwaves, and used this information along with Bragg's Law to confirm the structure of a given crystal lattice. We were able to very accurately confirm some of our measured results with the expected values, while in other experiments the expected value falls just outside the error bars of our measured quantities. Though we have qualitative and quantitative evidence to support the known theories and laws, we strive to better our experimental technique in order to more conclusively confirm expected values and relationships.

Contents

1 Introduction

1.1 Background

Optics, the science focused on the origin and propagation of light, can be divided into two major branches [**1**]. Geometrical optics concerns the principles that deal with the properties of lenses, mirrors, and other tools that manipulate light. Physical optics is the study of the nature and properties of light itself, such as diffraction, reflection, and refraction, among others. Although optics was originally purely applied as the study of visible light, in the 20th century optical methods began to develop for light throughout the electromagnetic spectrum, such as x-rays, ultraviolet rays, infrared waves, and microwaves.

Microwaves are a form of electromagnetic radiation with wavelengths much longer than visible light, their properties unable to be perceived by the human eye and only observable through microwave detectors. In the electromagnetic spectrum, they fall between radio and infrared waves [**2**]. Microwave frequencies range from 1.6 - 30 GHz which corresponds to their wavelengths from 187 - 10 mm, and their quantum energies from 0.66×10^{-5} to 0.12×10^{-3} eV.

In the past century, microwaves have proved to be extremely useful in a myriad of applications, including communication, navigation, radar, and heating [**3**]. Microwaves can be used in point-to-point communications to relay both digital and analog information such as voice, video, and data. They are also utilized in radar to detect the presence and locations of objects such as ships and aircrafts by analyzing the reflected microwaves that have been bounced off. Thus, this makes microwaves a vital component in national defense, air traffic control, and vehicular speed limit reinforcement. Additionally, because microwave absorption is manifested as heat, microwaves have been extremely advantageous for heating food, and is used in regular household appliances.

We seek to investigate the properties of microwaves through both geometrical and physical optics experiments. In our experiments, we will encounter and study microwave phenomena such as reflection, refraction, polarization, and diffraction. Our aim is to obtain qualitative and quantitative values concerning the relationships of microwaves and their properties, compare them to theoretical values and relationships, then analyze our methods through the accuracy of our calculated figures.

1.2 Apparatus

The relatively long wavelengths of microwaves allow for optics equipment larger than what would be used to study other forms of light such as x-rays or lasers. Much of the equipment have spacing on the order of several centimeters. Our basic setup, used for many of the experiments, includes a microwave transmitter and receiver placed on opposing sides of a goniometer, a round platform that allows for angle readings. The transmitter and receiver are slid onto the rotatable arms of the goniometer to enable their respective angle adjustment. The goniometer arm which the receiver is attached to also contains a potentiometer fastened in order for the receiver's position to be converted into a voltage readout on the computer. To generate output data, the microwave transmitter contains a diode which produces a linearly polarized microwave output with a wavelength of 2.85 cm [**4**]. This microwave is then detected by the receiver, which can relay both the microwave intensity and position information to LabView software. As the receiver gathers the relative intensity of the incoming microwave, LabView produces a readout graph of the detected intensity vs. the voltage reading of the potentiometer on the receiver. In order to obtain the angle position of a given intensity measurement, the user must first calibrate the goniometer every time data is acquired by taking the potentiometer's voltage reading at various angles of the receiver arm. After doing a linear fit of this relationship, the user can then convert the potentiometer voltage readings to angle positions. This allows a graph of intensity vs. angle position to be produced for a given data measurement. The setup is shown in Figure 1.

Most of the microwave experiments will require a piece of optics equipment, such as a double-slit plate or wax prism, placed in between the transmitter and receiver on the goniometer. When the receiver and transmitter are aligned across from each other such that the receiver detects maximum output signal from the transmitter, we will denote the angle positions of the transmitter and receiver as 0°and 180°, respectively. See Figure 2 for goniometer setup.

Because we take the angle of maximum detected intensity for many of our experiments, accuracy of both the alignment and calibration of the receiver and transmitter are crucial. Small offsets in the angles of the horns that direct the line of input and output microwaves may result in unaccounted for misalignment. We correct for this to the best of our ability by realigning the receiver and transmitter

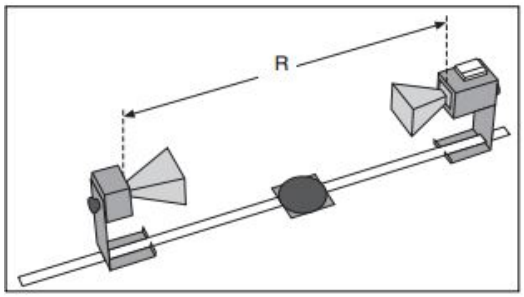

Figure 1: Basic microwave experiment set up.

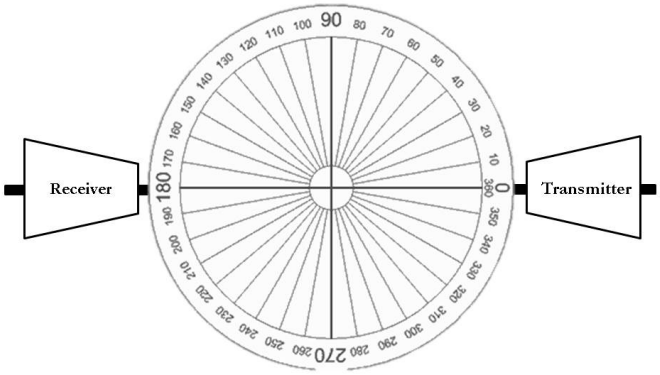

Figure 2: An overhead view of transmitter, receiver, and goniometer setup.

each day we take data; this is done by placing the transmitter at 0°and sweeping the receiver from 90°to 270°. We take the angle of maximum intensity that the receiver detects, and will call this angle the 180°angle for the receiver for the following experiments. Because much of the time the maximum falls at slightly different angles for successive sweeps, we note misalignment as a recurring measurement error, whose propagation will be discussed later. Calibration of the setup occurs each day we begin new data collection as well. To do this, the transmitter and receiver are aligned as detailed above, and the receiver arm is moved in five degree increments from 160°to 200°. The voltage reading, which the LabView software uses to track the position of the goniometer arm, is recorded for each increment, and the linear relationship between voltage reading and angle can thus be determined. Table 1 shows an example of a calibration that would be performed before an experiment, and Figure 3 shows an example of an angle vs. voltage graph that the calibration would produce. Because a new calibration is taken every day, the conversion numbers will not be explicitly shown in each of our experiments; however, voltage to angle conversion is implied in calculations, and each respective calibration error is discussed in the experiment.

Angle of transmitter (°)	LabView voltage readout
20	5.57
15	5.48
10	5.41
5	5.33
0	5.25
-5	5.17
-10	5.09
-15	5.01
-20	4.93

Table 1: An example of a calibration to convert voltage output to angle.

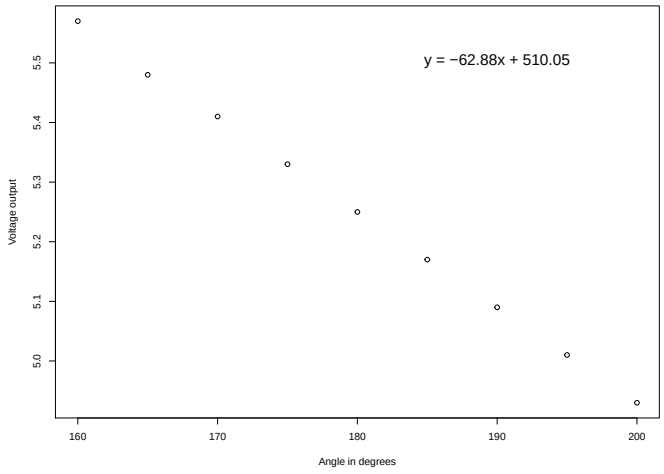

Figure 3: An example of a calibration plot.

2 Optics Experiments

2.1 Reflection

2.1.1 Theory

The law of reflection states that upon hitting a reflective surface, an incident ray of light is reflected at an angle equal to the angle of incidence [**5**]. This property can be derived from Fermat's principle, which states that light traveling between two points takes the path of least time. Thus, suppose we have light hitting a reflective surface like in Figure 4 [**6**].

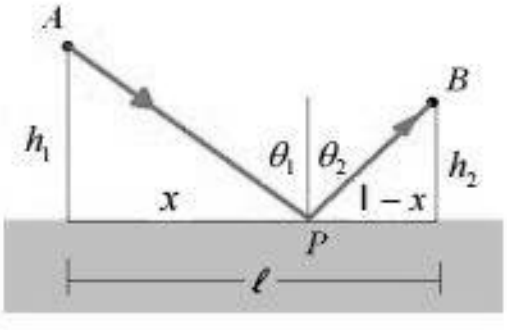

Figure 4: The path of a reflected light ray.

We can write the path length from A to B as

$$L = \sqrt{h_1^2 + x^2} + \sqrt{h_2^2 + (l-x)^2}$$

Then we can say that the time required to travel from A to B is written as

$$t = \frac{\sqrt{h_1^2 + x^2}}{c} + \frac{\sqrt{h_2^2 + (l-x)^2}}{c}$$

To find the path of least time, we take the derivative with respect to x and set it equal to zero. With some manipulation we can conclude that $\theta_1 = \theta_2$.

$$0 = \frac{dt}{dx} = \frac{x}{c\sqrt{h_1^2 + x^2}} + \frac{-(l-x)}{c\sqrt{h_2^2 + (l-x)^2}}$$

$$\frac{x}{c\sqrt{h_1^2 + x^2}} = \frac{(l-x)}{c\sqrt{h_2^2 + (l-x)^2}}$$

$$\sin\theta_1 = \sin\theta_2$$

$$\theta_1 = \theta_2 \tag{1}$$

In this experiment, we seek to confirm this theory.

2.1.2 Experimental Setup and Data Acquisition

We begin with our basic setup of the transmitter and receiver, and align and calibrate both of them. A reflective aluminum sheet is placed in between them such that the sheet itself is parallel to 0°and the plane is normal to 90°. Figure 5 gives a visual of the setup and how the angles of incidence and reflection are measured. The transmitter was moved from 10°to 55°in 5°increments. At each increment, the receiver was swept from 180°to 90°. We interpret the angle of reflection as the angle at which maximum intensity is recorded.

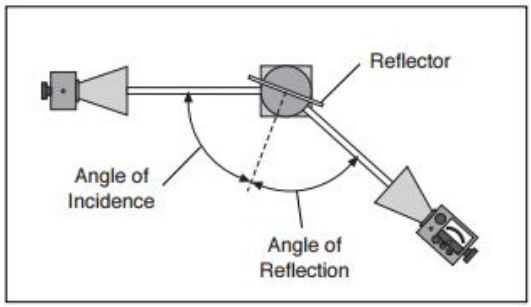

Figure 5: Interpretation of incidence and reflection angles.

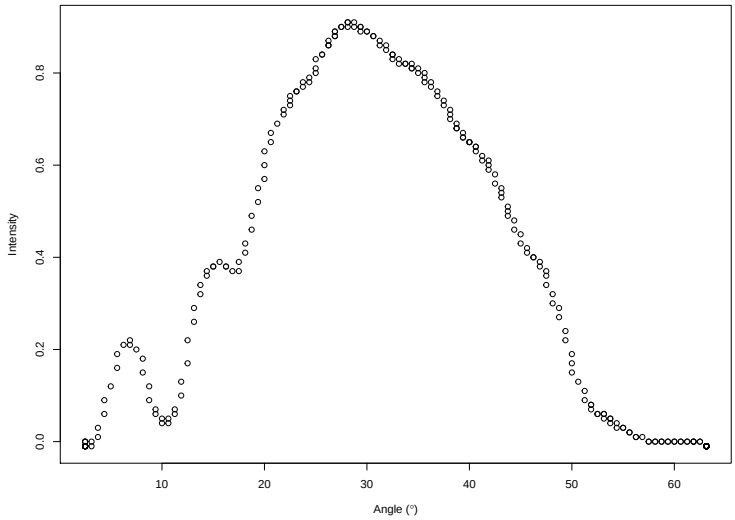

Figure 6: Intensity vs. angle for 30°angle of incidence.

2.1.3 Analysis, Results, and Discussion

Each measurement produced a plot of intensity versus angle of the receiver. Figure 6 shows this plot for a 30°angle of incidence. Because of the resolution limits of the apparatus and software, each data acquisition would have several voltage positions that contained the maximum observed intensity. Table 2 shows a data sample taken from the thirty degree sweep. To obtain the angle of reflection, all voltage readings which obtained the value of maximum intensity–in the sample case, 5.76, 5.76, and 5.77–were averaged together, and the averaged voltage was converted into the final reflection angle. This was done for each incidence angle that was measured. The results can be seen in Table 3, and a plot of the points overlayed with the theoretical relationship line can be seen in Figure 7.

The error bars for each point were calculated as follows. The error in the reflection angle measurement is a quadrature summation of the fitting error in the θ vs. voltage conversion, which is 0°; the error in voltage value from the LabView software, which corresponds to 0.97°; and the error in misalignment, which we set at 2°. The quadratic sum is approximately a 2.22°total error in the reflection angle and is shown as the y error bars in the plot. The error in incidence angle measurement is 0.5°to account for imprecision of aligning the transmitter goniometer arm with the angle tick mark, and is shown as the x error bars in the plot.

Looking at the graph we see that the residuals seem to follow a slight sinusoidal pattern. To investigate this, and its possible cause, further, more data points must be taken at smaller increments to obtain more precise data, and to see if the pattern holds under closer examination. Running a linear fit on our data, we see that for our reflection angle vs. incidence angle plot we obtain a slope of 1.0548 ± 0.0457, a y-intercept of -0.5206 ± 1.6236, and an adjusted R-squared value of 0.9834. Ultimately, we seek to retrieve a measured slope that contains the expected slope of 1 within its error bars, a y-intercept of 0, and an adjusted R-squared value of at least 0.99. Although our y-intercept is consistent with theoretical

Voltage (V)	Relative Intensity
5.73	0.86
5.73	0.87
5.74	0.88
5.74	0.88
5.74	0.89
5.74	0.89
5.75	0.9
5.75	0.9
5.76	0.9
5.76	0.91
5.76	0.91
5.77	0.91
5.77	0.9
5.78	0.9
5.78	0.9
5.78	0.89
5.79	0.89
5.79	0.89
5.8	0.88
5.8	0.88
5.81	0.87
5.81	0.86

Table 2: Sample taken from sweep of 30°reflection.

Angle of Incidence (°)	Angle of Reflection (°)
10	8.0 ±2.22
15	18.0 ±2.22
20	22.0 ±2.22
25	25.2 ±2.22
30	28.3 ±2.22
35	35.3 ±2.22
40	43.3 ±2.22
45	48.2 ±2.22
50	53.9 ±2.22
55	55.4 ±2.22

Table 3: Angles of reflection vs angles of incidence.

values, since our measured slope with error bars falls just above 1, we must reevaluate our data collection methods to minimize any possible cause and errors. We speculate that there was likely stray radiation picked up by the receiver as the microwaves from the source diverge, and eventually result in a range of reflection values rather than a single one. Because we observed that another aluminum sheet placed between the transmitter and receiver produced an even more incoherent signal than without, we will have to devise a better method for reducing the amount of stray radiation detected. Furthermore, since misalignment accounts for much of our y-axis error, it would be ideal if we could find a way to reduce the misalignment even further, either by switching instrumentation or improving our alignment methods. Our current data is revealing about linear relationship between reflection and incidence angles, but we strive to more accurately confirm our known theoretical relationship.

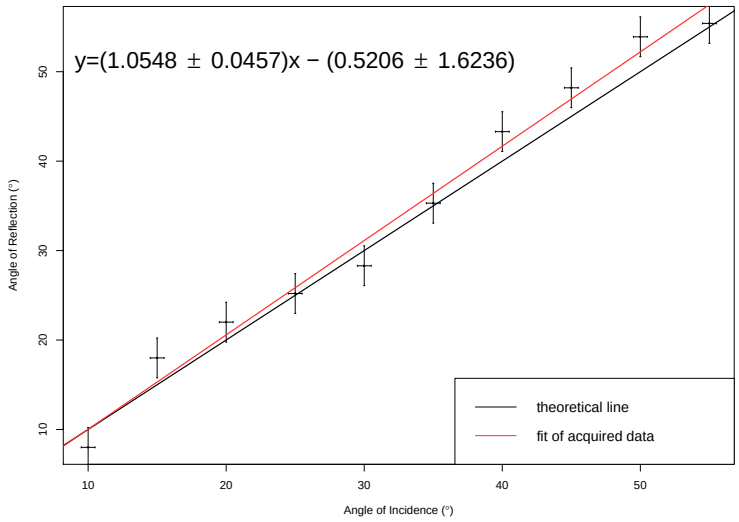

Figure 7: Angle of reflection vs angle of incidence with both regression fit and theoretical relationship line overlayed.

2.2 Refraction

2.2.1 Theory

The law of refraction, or Snell's Law, states that when light passes through two different media, it gets refracted in a way such that the ratio of the sine of the incidence angle to the sine of the refraction angle is equal to the inverse of their media's corresponding indices of refraction [**7**]. This can be visualized and summarized in Figure 8 and Equation 2.

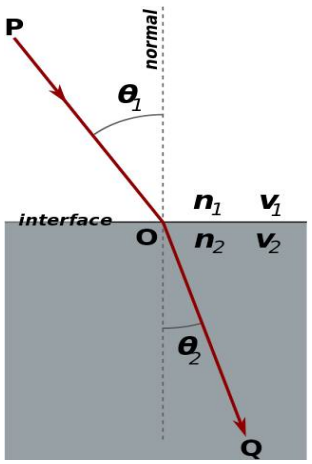

Figure 8: Visual of Snell's Law.

$$\frac{\sin\theta_1}{\sin\theta_2} = \frac{n_2}{n_1} \tag{2}$$

Like the law of reflection, the law of refraction can be derived from Fermat's principle [**8**]. Suppose we have light traveling from one medium to another, as in Figure 9. As in the law of reflection, we can write the path length from A to B as

$$L = \sqrt{h_1^2 + x^2} + \sqrt{h_2^2 + (l-x)^2}$$

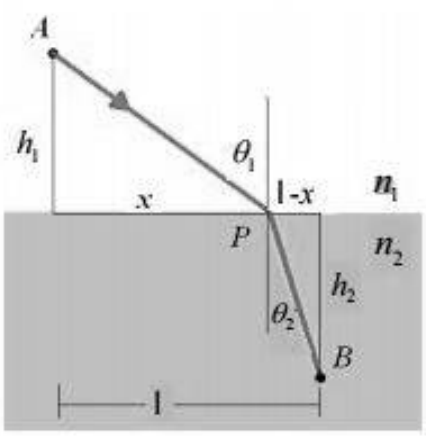

Figure 9: Visualization of refraction.

The time it takes to travel this length is

$$t = \frac{\sqrt{h_1^2 + x^2}}{\frac{c}{n_1}} + \frac{\sqrt{h_2^2 + (l-x)^2}}{\frac{c}{n_2}}$$

To minimize this, we take its derivative with respect to x and set it to zero.

$$0 = \frac{dt}{dx} = \frac{n_1 x}{c\sqrt{h_1^2 + x^2}} + \frac{-n_2(l-x)}{c\sqrt{h_2^2 + (l-x)^2}}$$

Manipulating this equation we obtain

$$\frac{n_1 x}{c\sqrt{h_1^2 + x^2}} = \frac{n_2(l-x)}{c\sqrt{h_2^2 + (l-x)^2}}$$

$$n_1 \sin\theta_1 = n_2 \sin\theta_2$$

$$\frac{\sin\theta_1}{\sin\theta_2} = \frac{n_2}{n_1}$$

We seek to determine the value of n_1, the refractive index of wax. We know from literature that n_2, the refractive index of air, is equal to 1.002 [**9**]. Our equation can then be written as

$$\sin\theta_2 = \frac{n_1}{1.002} \sin\theta_1 \tag{3}$$

What remains is to calculate n_1 by measuring θ_1 and θ_2.

2.2.2 Experimental Setup and Data Acquisition

We begin with our basic setup of the transmitter, receiver, and goniometer. As in Figure 10, in this experiment we place a half cylinder of wax in between the transmitter and receiver, with the rounded side facing the transmitter so that all incoming source rays hit the wax normal and are not refracted. Specifically, the source ray will leave the transmitter, hit the wax, and due to the cylinder shape facing the transmitter side, will always experience a change of medium interface normal to its original path. Thus, upon entering the wax, it will maintain its straight line of path, until it experiences another change of medium as it leaves the wax. This time, the interface of the wax and air results in a refraction of the microwave, which is then detected by the receiver by sweeping it from 90°to 270°. The angle of refraction is taken as the angle of maximum intensity which the receiver detects.

The transmitter was moved from 0°to 35°in 5°increments. At each increment, the receiver was swept from 90°to 270°. The angle at which the maximum intensity was taken is recorded as the angle of refraction.

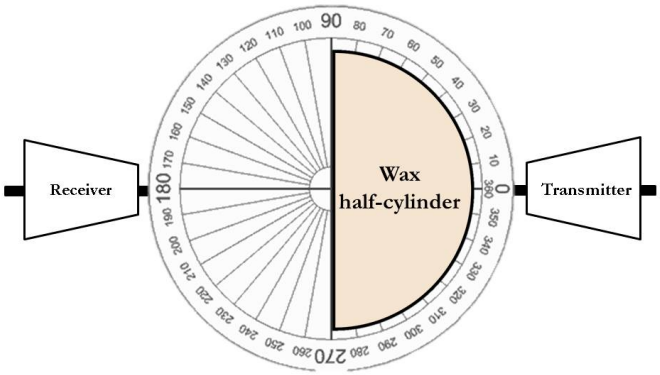

Figure 10: Visual of refraction experiment setup.

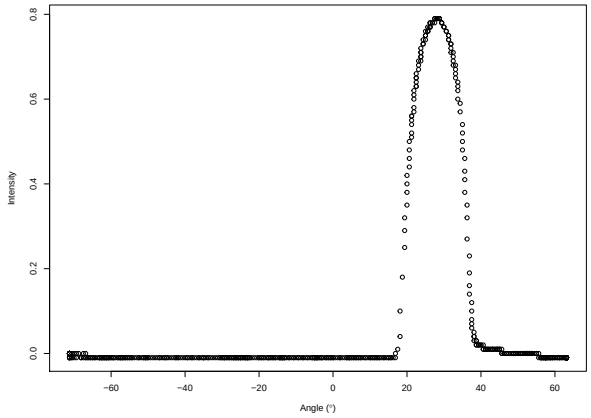

Figure 11: Intensity vs. angle plot produced for 30°angle of incidence.

2.2.3 Analysis, Results, and Discussion

Every measurement of incidence angle produced a plot of intensity vs. receiver angle as the receiver was swept. Figure 11 shows what the plot is for a 30°angle of incidence. As before, to obtain the angle of refraction, the maximum intensity was calculated from each incident angle sweep. All the voltage positions that gave this intensity value were averaged together then converted into a single angle position. This was done for each incidence angle that was measured. From literature, we know that the theoretical value of paraffin wax is approximately 1.445 [**10**]. Thus we can calculate the expected refraction angle from Equation 3 and compare it to our measured angle of refraction. The results are shown in Table 4.

The error in the angle of refraction was propagated similarly to the error in reflection angle; it is the quadrature summation of the θ vs. voltage calibration fitting error, the LabView voltage value error, and the misalignment error. The values for these are identical to the ones for reflection (See Section 2.1.3), and the total error in refraction angle is 2.22°. We observe that all of our measured refraction angles fall within two errors of the theoretical, and most fall within one error, indicating results as expected.

To obtain further perspective on our data, we plotted the sine of refraction angle vs. sine of incidence angle. According to Equation 3, our slope should equal to the theoretical slope of $\frac{1.445}{1.002} = 1.442$. Figure 12is a graph of our data points with a line of slope 1.442 overlayed on top. The error in sine of refraction angle is calculated from the propagation formula $\delta(\sin\theta_r) = (\cos\theta_r)\delta\theta_r$, using the value of $\delta\theta_r = 2.22°$ as calculated above. The error in sine of incidence angle is calculated using the same formula. We set $\delta\theta_i = 0.5°$, as in Section 2.1.3, to account for the imprecision in misalignment of the transmitter goniometer arm with the angle tick mark. $\delta(\sin\theta_r)$ and $\delta(\sin\theta_i)$ are then both calculated

Incidence θ (°)	Expected refraction θ (°)	Measured refraction θ (°)	Error in measured refraction θ	Difference in measured and expected refraction θ, divided by the error
0	0.0	-3.0	2.2	1.36
5	7.2	4.7	2.2	1.14
10	14.5	11.1	2.2	1.55
15	22.0	21.4	2.2	0.27
20	29.6	28.4	2.2	0.54
25	37.5	37.6	2.2	0.045
30	46.1	45.8	2.2	0.14
35	55.8	55.2	2.2	0.27

Table 4: Expected vs. measured refraction angles for each incidence angle.

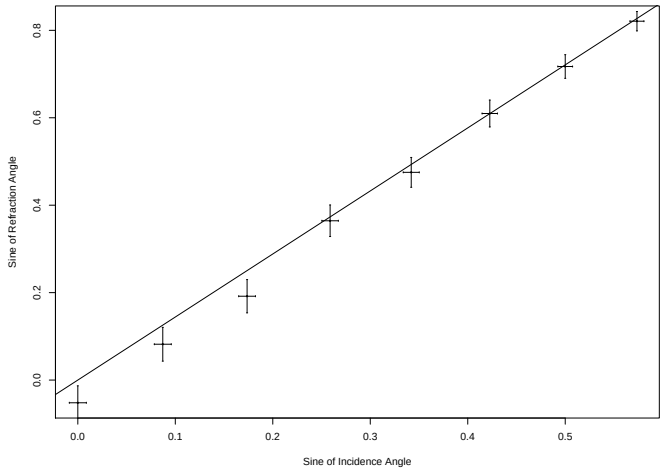

Figure 12: Sine of refraction angle vs. sine of incidence angle with line of slope 1.442 overlayed.

and drawn on the plot as the error bars in y and x, respectively.

Using linear regression we find that we obtain a slope of 1.542 ± 0.025, which corresponds to an n_{wax} value of 1.545 ± 0.025, and an adjusted R-squared value of 0.9984. Using our error value of 0.025, our slope is 4 errors off from our expected slope, but our high adjusted R-squared value indicates that our data fits a linear regression extremely well, despite its slope being slightly inaccurate. The high residuals and error differences in the first three data points leads us to speculate that there may be a factor affecting the accuracy of the measurement as the incidence angle becomes progressively smaller. However, Table 4 shows us that despite the slope being too high, all of our measured refraction angles are within two errors of the expected angles. To improve our refraction index result, we desire to further study this by smoothing out and eliminating inconsistencies in the wax half-cylinder edge, and also taking measurements to further improve the alignment of our wax. Stray radiation may be another factor, but because accuracy seems to improve with increased incidence angle, we will likely proceed by first investigating the structure and position of the wax.

2.3 Polarization

2.3.1 Theory

Microwaves from the transmitter are produced through a diode axis contained inside. Thus, any microwaves leaving the transmitter will be linearly polarized vertically because the diode axis is vertically aligned, as shown in Figure 13. The receiver also contains a diode that is vertically aligned. If we place a polarizer in between the transmitter and receiver, the polarizer will filter the incoming microwave, letting only a component of the incoming microwave pass through and be detected on the other side. The greater the angle of the polarizer, the less of the incoming microwave is able to pass through. See Figure 14 for a visual representation of polarization.

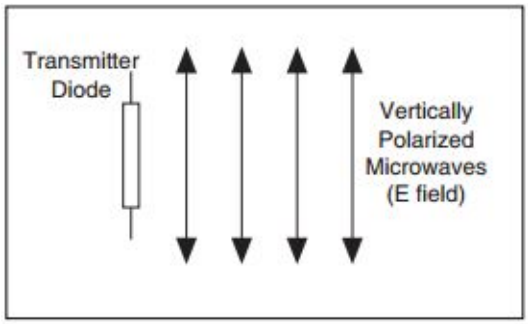

Figure 13: Vertically polarized microwaves.

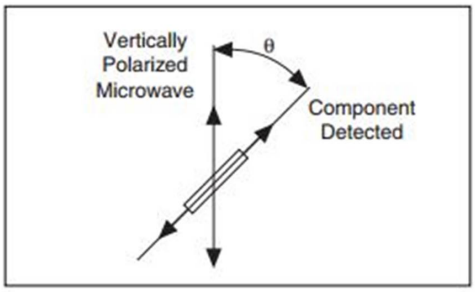

Figure 14: The receiver will only detect the component of the microwave that is able to pass through the rotated polarizer.

According to the theory, the intensity of the polarized microwave is proportional to the intensity of the unpolarized microwave multiplied by the cosine squared of the polarizing angle [**11**].

$$I = I_0 \cos^2 \theta \tag{4}$$

In this experiment, we seek to confirm this theory.

2.3.2 Experimental Setup and Data Acquisition

As usual, we begin with our basic setup of the transmitter and receiver. This time, we will place a polarizer in between them, as in Figure 15. The polarizer was rotated from 0°(with vertical polarizing slits) to 90°(with horizontal polarizing slits) in 5°increments. The angle of the polarizer was taken with a digital protractor. At each increment, the intensity that the receiver detected was recorded with the usual LabView software.

2.3.3 Analysis, Results, and Discussion

We have the intensity for each angle of polarizer that was taken. Figure 16 shows the measured intensity plotted against the angle of the polarizer, with the theoretical $\cos^2$ relationship plotted on top.

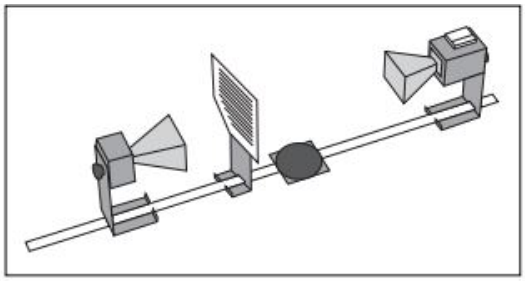

Figure 15: The setup of the polarization experiment.

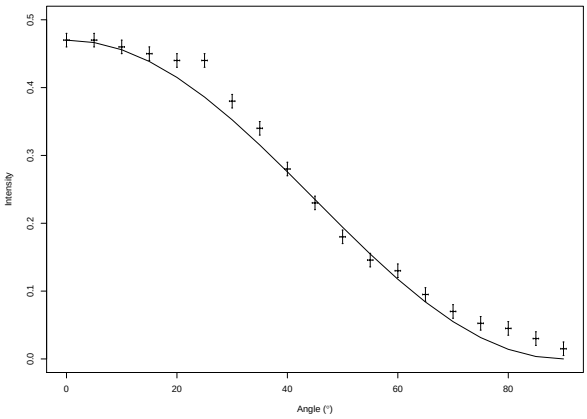

Figure 16: Intensity vs. angle with the expected relationship $I = I_0 \cos^2 \theta$ overlayed on top.

The error bars for this graph were calculated as follows. The LabView software displayed a ± 0.01 value for the δy (intensity) reading, and this constituted the error in the y axis. The digital protractor would oscillate in its reading at times, so we estimated the x axis an error of $\pm 0.5°$.

We ran a non-linear least squares fit on the data with the formula $I = I_0 \cos^n \theta$, and obtain an n value of 1.85 ± 0.075. With our error of 0.075, this is a 2 error difference from our anticipated value of n = 2. As this value does not fall within one error of our measured n value, we must continue to look for ways to improve our measurement and data collection methods. For this experiment, one method that we could consider is minimizing stray radiation that passes around rather than through the polarizer, which likely results in higher intensities than expected. This can be done by investing in a larger polarizer, or adding some sort of barrier to prevent the stray microwaves from reaching the detector.

2.4 Fabry-Perot Interferometer

2.4.1 Theory

In this experiment we will take a respite from the geometrical properties of microwaves and seek to determine a physical property of our investigated microwaves, the wavelength. To do this, we utilize a Fabry-Perot interferometer, which consists of the transmitter and receiver positioned with two parallel partial reflectors in between them (Figure 17). This time, we will not mount the receiver and transmitter on the goniometer arms but rather platform arms on which the receiver and transmitter can slide back and forth. This way, the transmitter and receiver remain at 180°across from each other, but the distance between them can be adjusted.

As shown in Figure 18, when the transmitter emits microwaves, some of the microwave will pass through to the detector, and some will reflect back and forth between the two reflectors before passing through. In our experimental setup, we are transmitting the microwave such that it is incident normal to the reflector, so that $\theta = 0$. Suppose the distance between the two partial reflectors is d. Then the path length difference between the microwaves that were passed through the reflectors and the ones that were reflected is $2d$. When the path length difference is equal to an integer number of the wavelength

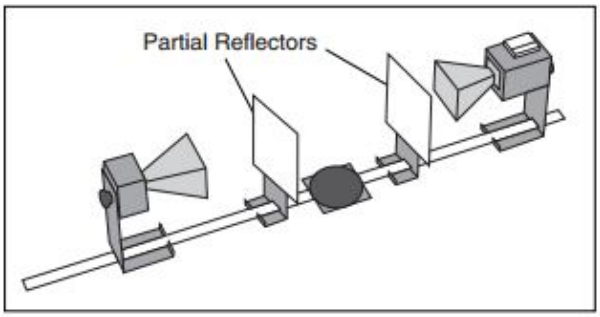

Figure 17: Setup of the Fabry-Perot interferometer.

of the microwave, maximum constructive interference occurs, and we will observe a peak in intensity in the detector.

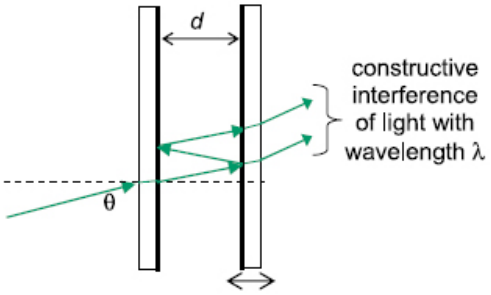

Figure 18: Visual of interference in the Fabry-Perot interferometer.

We can write this in the following equation:

$$n\lambda = 2d \text{ where } n = 1, 2, 3... \tag{5}$$

By adjusting the distance d and observing which ones give a peak intensity, we can infer that maximum constructive interference occurs at these distances. Since we have multiple intensity peaks, we use distance information from all the peaks through the following equation to calculate the wavelength:

$$\lambda = \frac{2d}{n} = \frac{2(d_{max} - d_{min})}{\text{number of peaks} - 1} \tag{6}$$

2.4.2 Experimental Setup and Data Acquisition

We start with the setup as in Figure 17. A potentiometer is connected to the receiver so that we can calibrate, this time, the voltage reading to the distance between the two plates. To do this, we take the voltage measurement at several known, measured distances and produce a linear regression for distance vs. voltage. After calibration, we slide the receiver from approximately 21.0 cm away from the transmitter to 40.0 cm away, slowly, while again using LabView to record the relative intensity of the received microwaves. Figure 19 shows the voltage to distance conversion plot, and equation 7 shows its linear regression equation.

$$d = (0.0795 \pm 0.0001)v + (-0.0723 \pm 0.0008) \tag{7}$$

Figure 20 shows the intensity vs. distance plot created after the voltage to distance conversion. The errors bars are shown on the peaks.

2.4.3 Analysis, Results, and Discussion

Figure shows multiple peaks as the receiver is slid from 21.0 cm to 40.0 cm, as expected. The peaks are enveloped by a $\frac{1}{d^2}$ curve, also as expected, as the intensity decreases inversely proportional to the square of the distance.

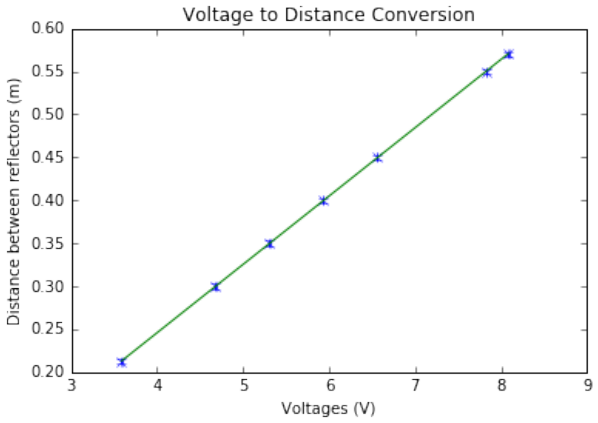

Figure 19: Voltage to distance conversion plot for Fabry-Perot.

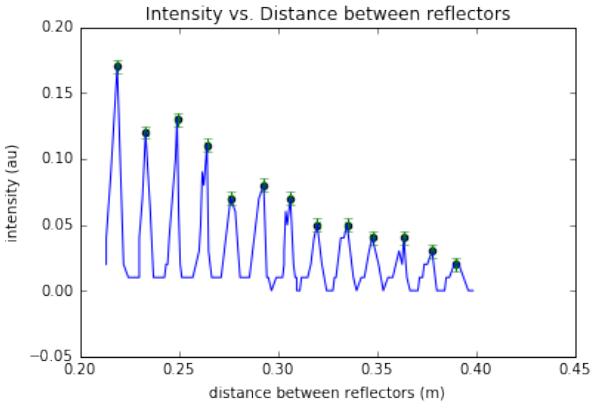

Figure 20: Intensity vs. distance for Fabry-Perot.

Our error bars were calculated as follows. The error in d was a quadrature summation of the errors of the voltage to distance conversion, which was 0.0001 and 0.0008; the error in the ruler measurement of receiver position, which was 0.05; and error in voltage readout of the potentiometer on the LabView software, which was 0.005. The summation turns out to be 0.7 mm, as shown in the x-axis error bars. The error in intensity are due to fluctuations in intensity of the LabView reading, which was 0.003 in magnitude, and is shown as the y-axis error bars.

Using equation 6, we calculate the wavelength of the microwave to be:

$$\lambda = \frac{2(0.1898 - 0.0188)}{12} = 0.0285 \pm 0.0001\text{m} \tag{8}$$

As mentioned in section 1.2, the equipment manufacturers specify that the transmitter produces a wavelength of 2.85 cm. Thus, our calculated wavelength agrees with our expected value.

2.5 Bragg's Law

2.5.1 Theory

Given a crystal structure, Bragg's Law details the relationship between the structure and the incident electromagnetic rays that hit and are scattered off the structure [**12**]. Figure 21 gives visual context for this principle.

An incoming microwave will hit a plane of atoms in the crystal lattice and reflect off. But, as seen in Figure 21, the path traversed by the microwave that hits the layer below it will be $2d\sin\theta$ longer than the path traveled from the incident microwave on the top layer. Because of this path length difference, interference will occur in the reflected microwaves. If the incident microwaves happen to come in at a certain angle, maximum constructive interference will occur between the two reflected microwaves, and peaks of intensity will be observed. This happens when the path length difference is equal to an

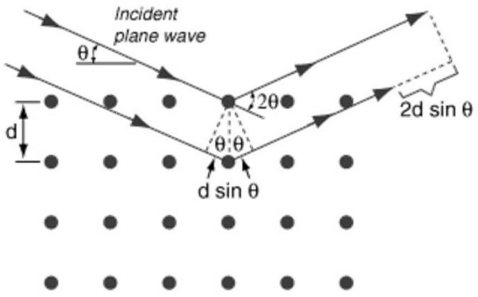

Figure 21: Theory behind Bragg's Law.

integer number of the wavelength of the microwave. The relationship between the angle of the incident microwave and the structure of the crystal lattice is known as Bragg's Law:

$$n\lambda = 2d\sin\theta \tag{9}$$

Where n is the integer number, λ is the wavelength of the microwave, d is the distance between adjacent planes, and θ is the incidence angle of the microwave with respect to the observed plane. We can measure the incidence angle, and we have calculated a value of λ from the Fabry-Perot experiment. We will start at values of $n = 1$ and increase by every integer with each observed peak of intensity. With this information, we seek to calculate d.

In our experiment we will be observing three planes. Figure 22 depicts the three planes that we will be investigating. Each plane has a different d value, the distance between two adjacent planes for a given plane of study; with geometry, we can use each measured d value calculate a, the distance between the atoms in the 100 plane. We can then measure the distance a directly on our crystal lattice, and then compare our calculated a values to our measured one. For a simple cubic lattice, the relationship

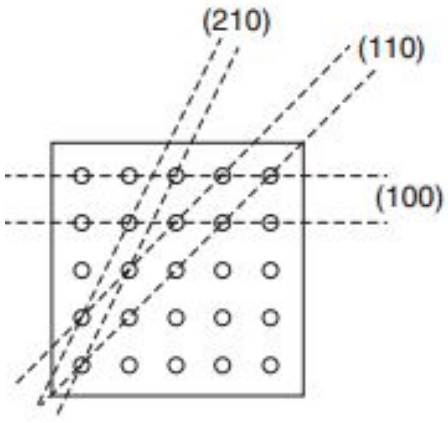

Figure 22: Three different planes being investigated, labeled 100, 110, and 210.

between the distance d between adjacent planes and the distance a between atoms in the 100 plane is [**13**].

$$d_{hkl} = \frac{a}{\sqrt{h^2 + j^2 + l^2}} \tag{10}$$

Therefore, for each individual plane of study, we can write:

$$d_{100} = \frac{a}{\sqrt{1^2 + 0^2 + 0^2}} = a \tag{11}$$

$$d_{110} = \frac{a}{\sqrt{1^2 + 1^2 + 0^2}} = \frac{a}{\sqrt{2}} \tag{12}$$

$$d_{210} = \frac{a}{\sqrt{1^2 + 1^2 + 1^2}} = \frac{a}{\sqrt{5}} \tag{13}$$

2.5.2 Experimental Setup and Data Acquisition

We begin with our basic setup of the transmitter and receiver, this time placing a cubic lattice made of styrofoam and aluminum balls, which will serve as our atoms, between them. Thus we will have a setup such as Figure 23. The lattice is positioned such that the plane in investigation is always normal

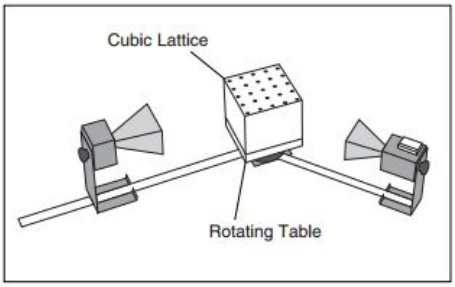

Figure 23: Setup of Bragg experiment.

to the 270°mark. Each measurement is taken by moving the transmitter 1°clockwise and the receiver 1°counterclockwise, then taking the intensity value recorded by the receiver at that angle. We took measurements moving the transmitter clockwise every 1°from 0°to 60°, and the receiver respectively, from 180°to 120°, for all of the planes.

2.5.3 Analysis, Results, and Discussion

Our measurements produce intensity vs. angle plots for all of the planes, as shown in Figures 24, 25, and 26; the angle is the transmitter angle measured from 0°. All of the plots begin with an extremely high intensity value which falls off by 15°; these are taken to be a result of stray radiation picked up due to the small angle positions of the receiver and transmitter, and will not be included in our analysis of maximum intensity peaks. In the plane 100 plot, we observe two maxima that we will use: one at

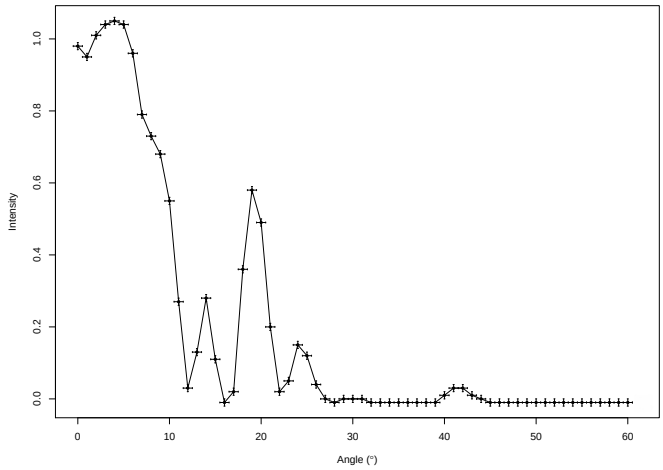

Figure 24: Intensity vs. angle for plane 100.

$19° \pm 0.5°$ and one at $41.5° \pm 0.5°$. The two shorter peaks next to the 19°peak are assumed to be a result of extra interference resulting from the 19°intensity peak, and will be disregarded. Because the error bars for plane 210 may make the data difficult to discern, we include a plot for plane 210 without error bars.

In the plane 110 plot, we observe a maximum at $27° \pm 0.5°$. Last, in the plane 210 plot, we are unable to observe any significant peaks. We resolve to use data from plane 100 and 110 to calculate the expected distance between our "atoms".

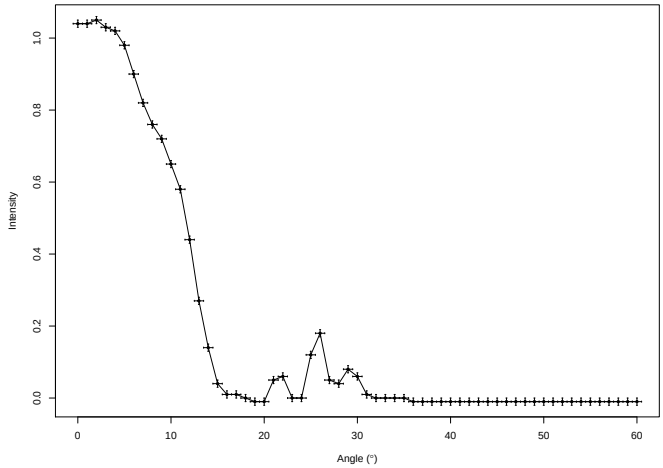

Figure 25: Intensity vs. angle for plane 110.

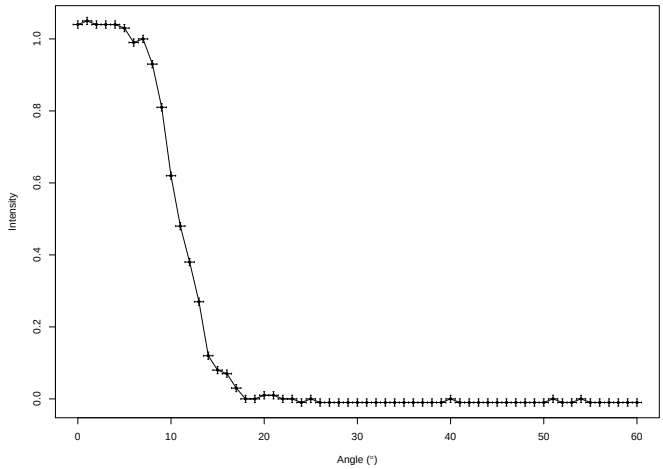

Figure 26: Intensity vs. angle for plane 210.

The error bars for each plot are calculated similarly to the errors for the previous experiments. As in reflection and refraction, we estimated a 0.5°error in the incidence angle to account for imprecision of alignment of the goniometer arm with the angle tick mark, and is shown as the x-axis error bars. The LabView software shows a 0.01 δy error in intensity reading, so we attribute a 0.01 intensity error as shown in the y-axis error bars.

To calculate a for the three different planes, we simply use Bragg's Law and equations 11 and 12 to obtain a as shown in equations 13 and 14.

Thus, the calculation for a using plane 100 data would be:

$$a = \frac{n\lambda}{2\sin\theta} \tag{14}$$

Our error propagation for plane 100 data is then:

$$\delta a = a\frac{n}{2}\sqrt{(\frac{\delta\theta\cos\theta}{\sin\theta})^2 + (\frac{\delta\lambda}{\lambda})^2} \tag{15}$$

Our a calculation using the plane 110 data:

$$a = \frac{\sqrt{2}n\lambda}{2\sin\theta} \tag{16}$$

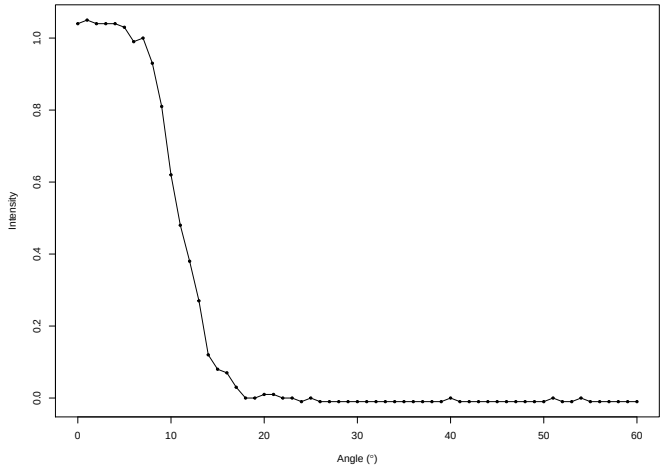

Figure 27: Intensity vs. angle for plane 210 without error bars.

And the error calculation for the plane 110 data is:

$$\delta a = \sqrt{2} a \frac{n}{2} \sqrt{(\frac{\delta\theta \cos\theta}{\sin\theta})^2 + (\frac{\delta\lambda}{\lambda})^2} \tag{17}$$

These calculations are shown in Table 5. Our measured spacing, or theoretical value of a, is 4.31 ± 0.05 cm, and our λ value is 2.85 ± 0.01 cm from our Fabry-Perot experiment (Section 2.4).

Investigated plane	n	θ of intensity peak	d (cm)	a (cm)	Theoretical a value (cm)
100	1	19 ± 0.5	4.37 ± 0.012	4.37 ± 0.012	4.31 ± 0.05
100	2	41.5 ± 0.5	4.30 ± 0.019	4.30 ± 0.019	4.31 ± 0.05
110	1	27 ± 0.5	3.14 ± 0.011	4.43 ± 0.015	4.31 ± 0.05

Table 5: Calculated d and a values for investigated planes alongside measured a value.

Table 5 shows us that the a values for both peaks of the plane 100 data fall within the error bars of our measured a value of 4.31 ± 0.05 cm. However, we observe that the a value for the plane 110 plane does not. As there is more error involved in the alignment of the crystal lattice for the investigation of plane 110, we can speculate that this may be due to misalignment. Another possibility for the discrepancy in data is more stray interference occurring when examining plane 110; one possible solution to mitigate this issue is adding an aluminum sheet between the transmitter and receiver, parallel to the 270°line, and observing whether or not this minimizes stray radiation. Furthermore, as our plane 210 data failed to show any significant peaks, we must also look into recollection of this data in the case of any misalignment or stray radiation issues that we may be able to minimize. Another possibility is to change or fix our cubic lattice, in the case of any structural inconsistencies that we may have overlooked.

2.6 Single-Slit Diffraction

2.6.1 Theory

In this experiment, we investigate the properties of a microwave passing through a single slit of comparable length to the wavelength of the microwave. Figure 28 shows a schematic for microwaves passing through the slit. According to Huygen's principle, every point on a wavefront–in this case, the slit opening–can be considered as a source of wavelets [**14**]. As the wavelets are propagated toward the detector on the right, however, they will undergo interference due to their path length difference. If we let the length of the single slit be denoted as w, and the angle from the normal of the plane of the detector be denoted as θ, we can use trigonometry and the small angle approximation to calculate the path length

difference between waves coming from opposite ends of the slit at a given point on the detector as $\frac{w \sin\theta}{2}$. As in the Fabry-Perot and Bragg's law experiments, we will observe maximum constructive interference at points on the detector when the path length difference is equal to an integer number of the wavelength. Likewise, we will observe maximum destructive interference when the path length difference is equal to a half-integer multiple of the wavelength. These two conclusions can be summarized with equations 18 and 19, respectively.

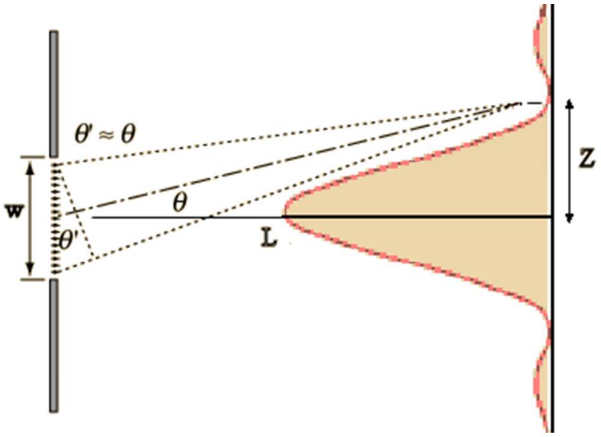

Figure 28: Visual schematic for single-slit diffraction.

$$\frac{w \sin\theta}{2} = n\lambda \text{ where } n = 1, 2, 3... \text{ (constructive)} \tag{18}$$

$$\frac{w \sin\theta}{2} = (n + \frac{1}{2})\lambda \text{ where } n = 1, 2, 3... \text{ (destructive)} \tag{19}$$

Thus, at different points in detector position, we will observe various intensities resulting from the summation of the propagating wavelets. The diffraction should produce a pattern similar to the one depicted in Figure 28. The equation relating intensity and the angular position θ can be written as follows:

$$I(\theta) = \frac{\sin^2(\frac{\pi w \sin\theta}{\lambda})}{(\frac{\pi w \sin\theta}{\lambda})^2} \tag{20}$$

We seek to investigate the phenomenon of single-slit diffraction with varying slit widths and lengths. We seek to test our experimental results against a ROOT simulation which will give us an expected pattern for single-slit diffraction. By overlaying our diffraction patterns with what the simulation gives us, we can analyze our experimental results against the theoretical pattern of the simulation.

2.6.2 Experimental Setup and Data Acquisition

We begin with our setup of the transmitter and receiver placed on opposite ends of the goniometer. As before, we calibrate and align our setup to obtain the angle vs. voltage relationship and to find the maximum intensity position, respectively. On the goniometer we then place a stand, normal to the 0°mark, that can hold an aluminum sheet with a rectangular slit cut out in the middle. We keep the transmitter at 0°, and we detect the transmitted microwaves that have passed through the slit by sweeping the detector from 90°to 270°. We perform this procedure for aluminum sheets with slit widths of 3.05 ± 0.03 cm, 8.76 ± 0.03 cm, and 18.86 ± 0.03 cm.

The ROOT simulation draws a lattice of wave sources in an input area of a rectangular slit. These sources are spaced $\frac{1}{10}$ of a wavelength, of 2.85 mm, apart. When the parameters of the experiment setup–such as the width and length of the slit, and the distances from the source to the slit and the slit to detector–are passed into the simulation, the simulation calculates the sum of all of the wavelets at each given detector position. In doing this, the simulation creates a plot of the expected diffraction pattern that we can compare with the pattern that we obtained from the detector. We create simulations for each of the slit widths that we tested with the detector.

2.6.3 Analysis, Results, and Discussion

We create three different plots for each slit width: a plot with the raw data, a plot with the detector's voltage converted to angle, and a voltage-angle converted plot with the simulation overlaid on top. Figures 29 to 37 to show these plots for each of the investigated slit widths.

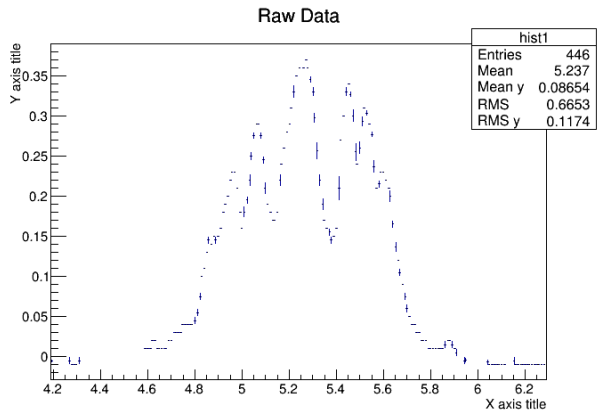

Figure 29: 3.05 cm slit width, raw plot.

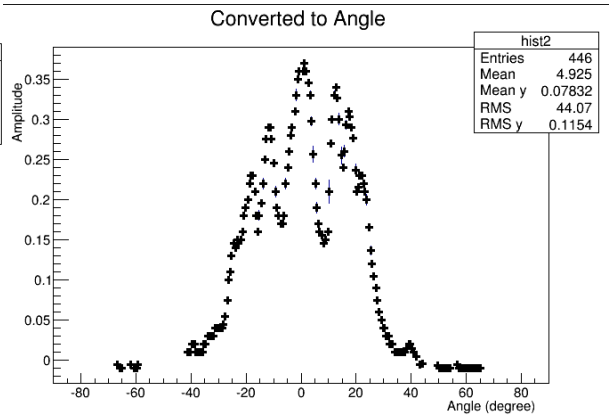

Figure 30: 3.05 cm slit width, converted to angle plot.

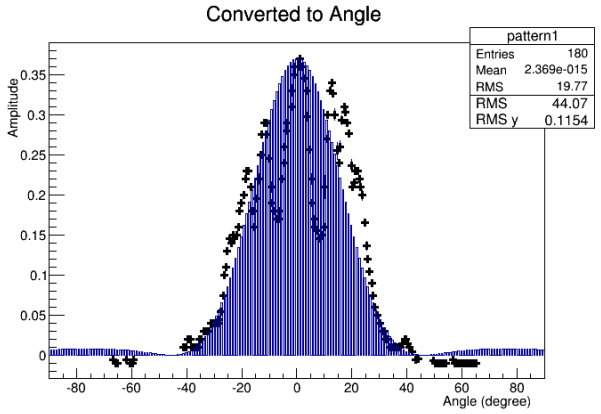

Figure 31: 3.05 cm slit width, overlaid with simulation plot.

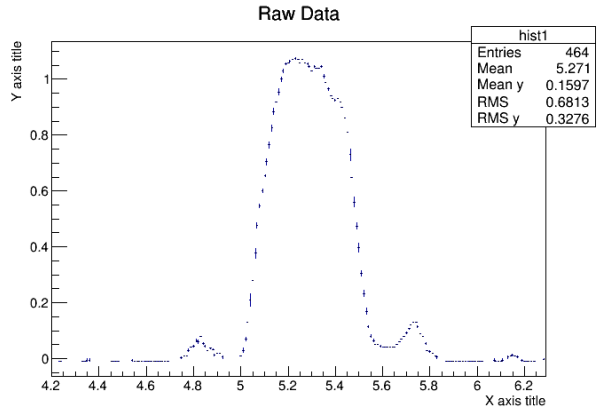

Figure 32: 8.76 cm slit width, raw plot.

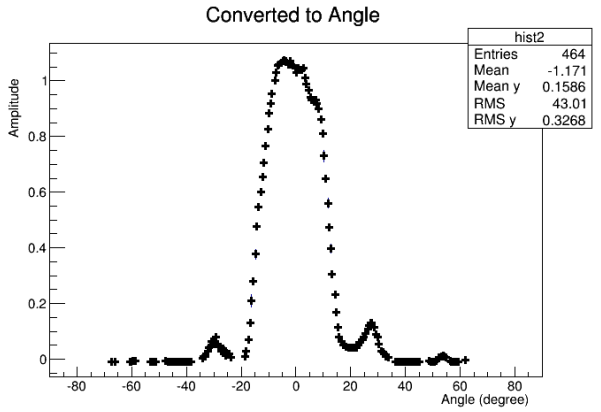

Figure 33: 8.76 cm slit width, converted to angle plot.

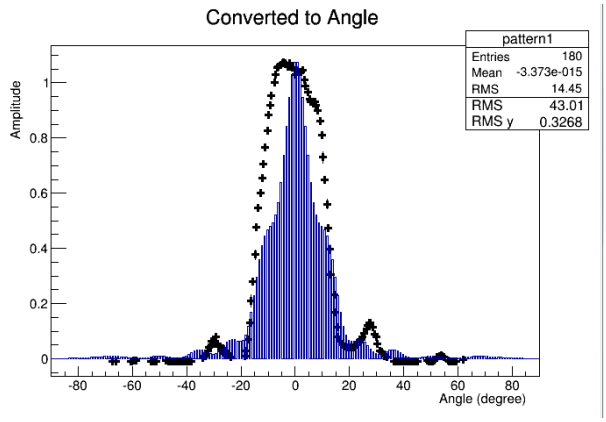

Figure 34: 8.76 cm slit width, overlaid with simulation plot.

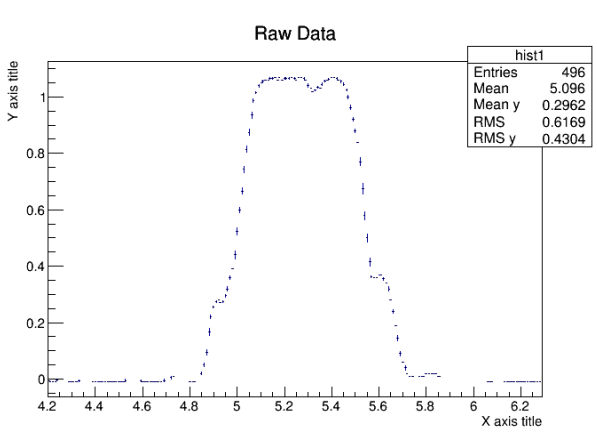

Figure 35: 18.86 cm slit width, raw plot.

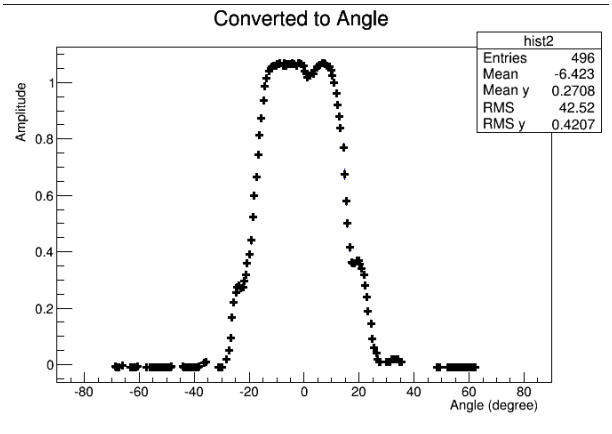

Figure 36: 18.86 cm slit width, converted to angle plot.

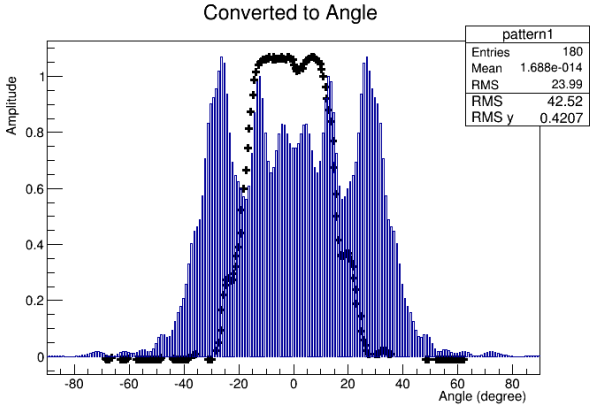

Figure 37: 18.86 cm slit width, overlaid with simulation plot.

The error bars in these plots are calculated as follows. The x-axis error bars are a quadrature summation of the errors in the voltage-angle calibration and the uncertainty in the voltage reading on LabView, the latter of which is shown as a δx on LabView. The y-axis error bars are the errors in intensity readings, which are shown as a δy on LabView.

We observe that the peaks of all the plots are centered at almost exactly $0°$, allowing us to infer that misalignment is likely not an issue in any discrepancies we see between the simulations and the our collected data. In the 3.05 ± 0.03 cm slit, we can see that we obtain three peaks instead of one large one as predicted, indicating that additional diffraction is occurring. As adjusting the distance between the source and the slit still produced these additional peaks, we speculate it may be that the slit is so narrow that the wavefront is somehow disrupted, resulting in more of a double-slit pattern than the expected single-slit one. The 8.76 ± 0.03 cm slit width produces a wider peak than predicted, and higher maxima and lower minima in the smaller diffraction peaks. The largest slit, 18.86 ± 0.03 cm width, produced no diffraction patterns and instead generated a large central peak. We speculate that this may be due to the extremely wide slit width in comparison to the wavelength of the microwave; the waves may not have experienced any diffraction or interference as they reached the detector but rather were merely passed through the slit and cut off at the edges. To further examine these discrepancies, we propose adjusting the distance from the source to the slit and from the slit to the detector to see if these are contributing factors to our results. Otherwise, we could increase the length of the aluminum sheet on which the slit is cut out, to prevent stray radiation from passing around the edges of the sheet and interfering with the final diffraction pattern on the detector.

2.7 Double-Slit Diffraction

2.7.1 Theory

In 1801, Thomas Young performed his famous double-slit experiment which demonstrated the wavelike nature of light [**15**]. In this experiment, we seek to replicate his methods to observe the diffraction that results from waves passing through two slits, with widths comparable to the wavelength of our observed light. Consider a microwave hitting a sheet with two identical slits cut out as in Figures 38 and 39.

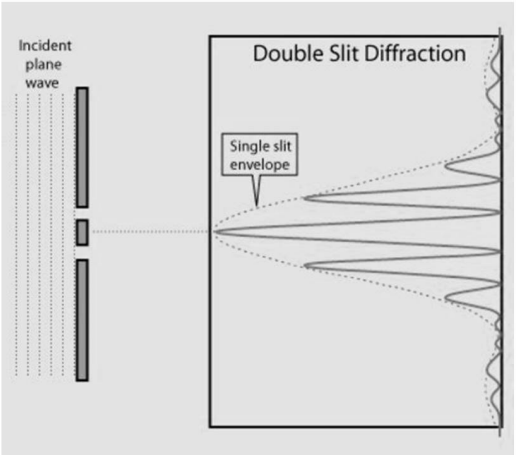

Figure 38: Light hitting double slits and producing an interference pattern.

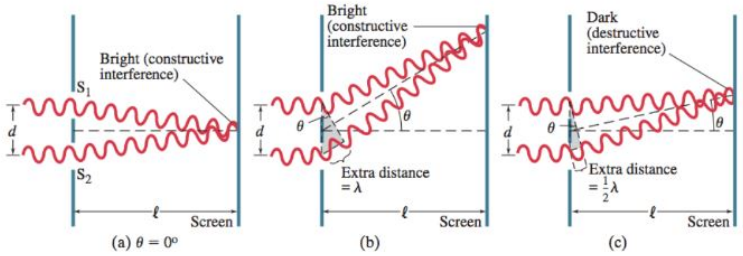

Figure 39: Constructive and destructive interference resulting from the two wave sources (double slits).

As seen in Figure 39, the interference of the waves coming from each slit produces alternating bright and dark fringes in positions where maximum constructive and destructive interference occurs, respectively. As in the single-slit experiment, this is due to the path length difference in the propagation of two waves coming from different wavelet sources (Huygen's principle), which is in this case, the two slits. Thus, let d be the distance between the two slits and θ be the angle with respect to the normal of the sheets. Maximum constructive and destructive interference occurs when the path length difference at a point on the detector, which can be written as $d\sin\theta$, is equal to an integer and half-integer number of wavelengths, respectively. We can write the equations for constructive and destructive interference as follows:

$$d\sin\theta = n\lambda \text{ where } n = 1, 2, 3... \tag{21}$$

$$d\sin\theta = (n + \frac{1}{2})\lambda \text{ where } n = 1, 2, 3... \tag{22}$$

If we let the slit width be w, we can further see that the double-slit diffraction pattern is governed by the following equation:

$$I(\theta) = \cos^2(\frac{w\pi\sin\theta}{\lambda}) \times \frac{\sin^2(\frac{\pi w\sin\theta}{\lambda})}{(\frac{\pi w\sin\theta}{\lambda})^2} \tag{23}$$

Which allows us to observe that the diffraction pattern produced by a double-slit is in fact enveloped by the diffraction pattern of a single-slit of the same width, as Figure 38 implies. We seek to observe this

property in our experimental data as well. As in single-slit diffraction, we expect the central maximum of the envelope to narrow as the slit width gets larger. Moreover, as the slit separation increases, we expect to observe more peaks.

As in single slit, we desire to test our experimental results against a ROOT simulation which allows us to pass parameters such as slit width and separation in order to make a predicted plot of the diffraction pattern. We will again overlay the simulated and experimental data to analyze our methods and results.

2.7.2 Experimental Setup and Data Acquisition

The setup and data acquisition of this experiment is identical to the single-slit experiment (See Section 2.6.2), with the exception that we are now using aluminum sheets with double slits as opposed to single slits. The transmitter passes microwaves, which then goes through the double slits, and we obtain the data by sweeping the detector from 90°to 270°. Figure 40 shows a visual of the double-slit setup.

We test the following double-slits having: width of 3.05 ± 0.03 cm each and separation of 6.08 ± 0.03 cm, width of 6.08 ± 0.03 cm each and separation of 11.97 ± 0.03 cm, and width of 8.76 ± 0.03 cm each and separation of 8.76 ± 0.03 cm. We pass the respective parameters into the ROOT simulation to obtain our expected patterns.

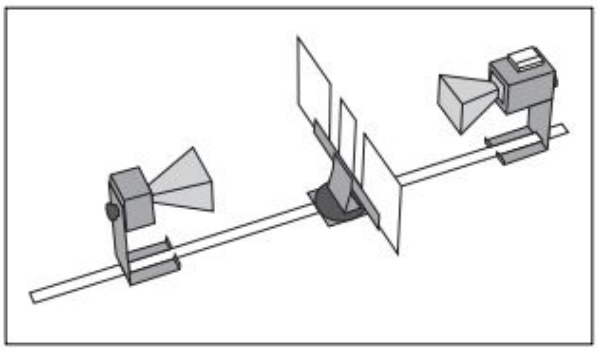

Figure 40: Setup of the double-slit experiment.

2.7.3 Analysis, Results, and Discussion

As in the single-slit experiment, we produce plots of raw data, plots with the detector voltage converted to angle, and voltage-angle converted plots with the simulation overlaid on top. Figures 41 to 49 show these plots for all of the investigated double slits. The errors are calculated the same as in the single-

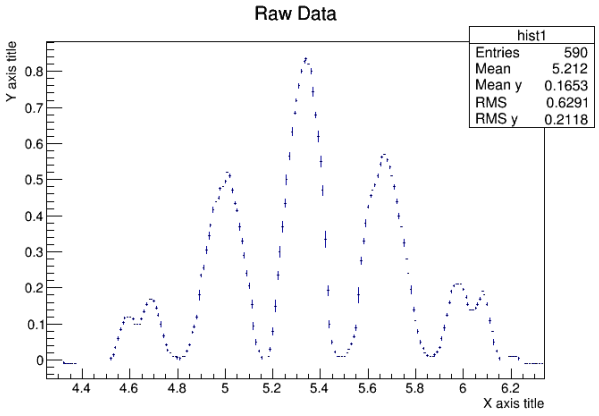

Figure 41: 3.05 cm slit width, 6.08 cm slit separation, raw plot.

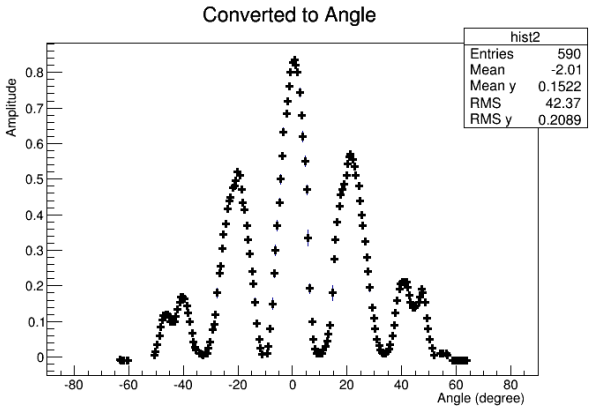

Figure 42: 3.05 cm slit width, 6.08 cm slit separation, converted to angle plot.

slit experiment. The x-axis error bars are a quadrature summation of the errors in the voltage-angle calibration and the uncertainty in the voltage reading on LabView. The y-axis error bars are the errors in intensity readings, which are shown as a δy on LabView. Also as in the single-slit experiment, we note

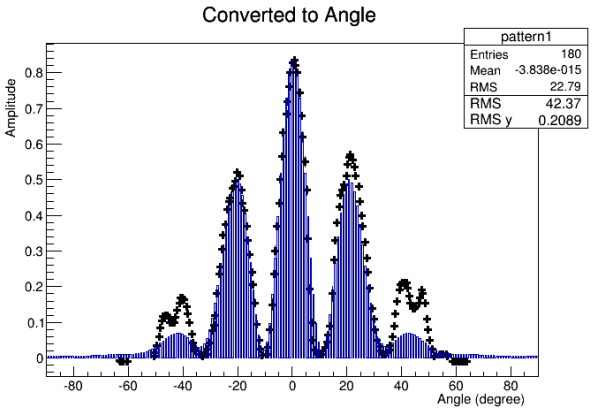

Figure 43: 3.05 cm slit width, 6.08 cm slit separation, overlaid with simulation plot.

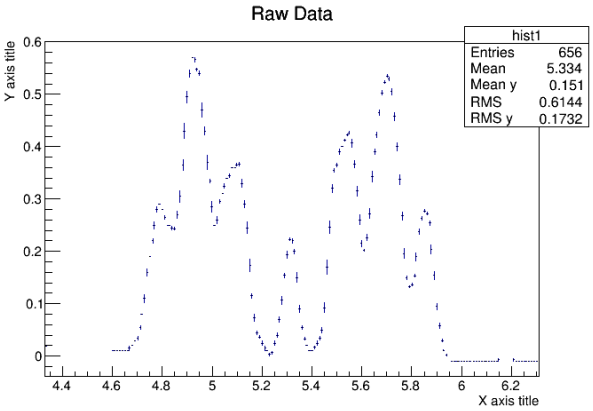

Figure 44: 6.08 cm slit width, 11.97 cm slit separation, raw plot.

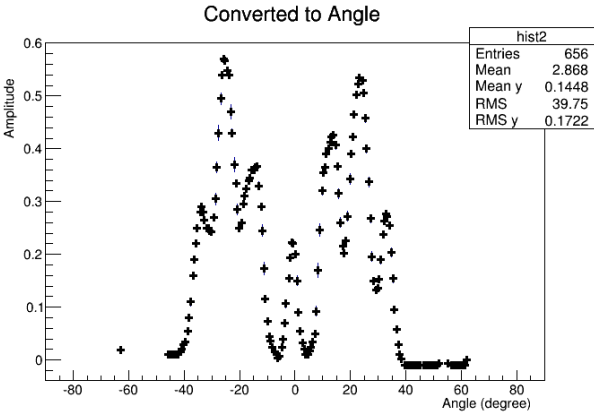

Figure 45: 6.08 cm slit width, 11.97 cm slit separation, converted to angle plot.

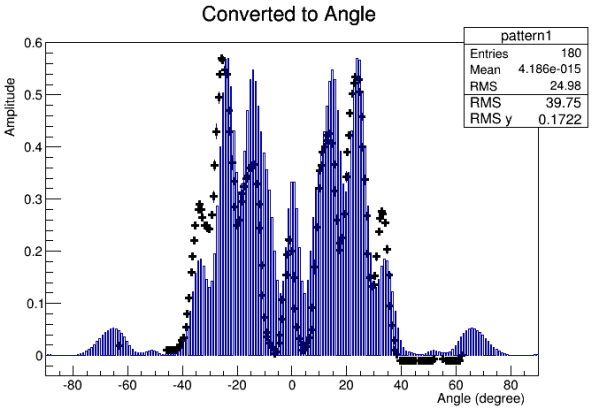

Figure 46: 6.08 cm slit width, 11.97 cm slit separation, overlaid with simulation plot.

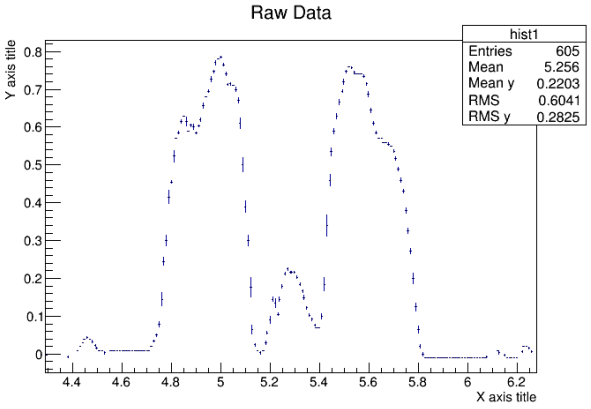

Figure 47: 8.76 cm slit width, 8.76 cm slit separation, raw plot.

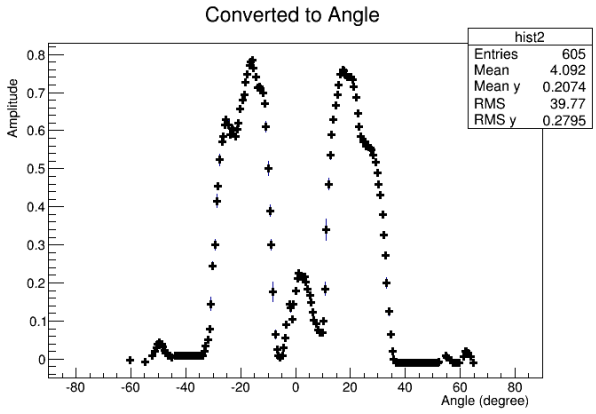

Figure 48: 8.76 cm slit width, 8.76 cm slit separation, converted to angle plot.

that the central peaks of the graphs fall almost exactly at 0°, indicating that misalignment is unlikely to be a significant source of error.

We observe that as the slit separation increases, the number of peaks increases, which is an expected result. The slit separation of 6.08 ± 0.03 cm produces 5 peaks; 8.76 ± 0.03 cm, 7 peaks; and 8.76 ± 0.03 cm, 9 peaks. The slit with width of 3.05 ± 0.03 cm each and separation of 6.08 ± 0.03 cm adhered the

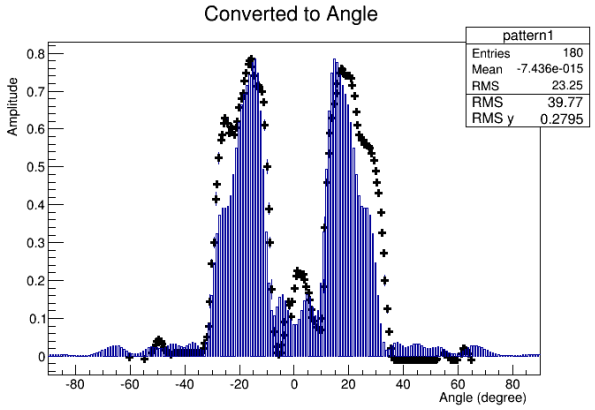

Figure 49: 8.76 cm slit width, 8.76 cm slit separation, overlaid with simulation plot.

most closely to our expected results, with the peaks adjacent to the central peak a bit higher than we expect. We speculate this may be due to additional interference from the stray radiation that passed around the aluminum sheet rather than through the slits. The slits of width of 6.08 ± 0.03 cm each and separation of 11.97 ± 0.03 cm approximately agreed with the simulation, but with the peaks adjacent to the center turning out much lower than expected, and absent peaks at approximately 65°. However, as 65°is close to the edge of the aluminum sheet, it is likely more subject to the stray radiation coming from the sides of the sheet, and we hypothesize that this may result in some undesirable destructive interference. Last, the slits of width 8.76 ± 0.03 cm each and separation of 8.76 ± 0.03 cm align well with the simulation; however, we observe one central peak near 0°, while the simulation gives us a minimum at 0°and two smaller adjacent peaks next to it. The cause of this discrepancy is unknown and we will likely have to do further tests into our experimental methods – such as adjusting the distances between our source to slit and slit to detector, or devising a means to block off stray radiation – to investigate this further.

3 Summary and Conclusion

Our seven experiments involving microwaves–reflection, refraction, polarization, Fabry-Perot interferometry, Bragg's Law, and single and double slit diffraction–allowed us to directly observe both geometric and physical properties of microwaves on a physically larger scale than many other optics experiments permit. Although we were able to confirm some laws and quantitative results, other expected values fell just outside the error bars of our measured values. As this prevents us from decisively deducing the theoretical laws from our experimental results, we are motivated to go back and re-evaluate our experimental methods or data analysis to see if our results and conclusions are valid. We conclude that while our methodology and analysis are reasonable, more can be done to ensure the accuracy and soundness of our results. Regardless, performing these experiments and analyzing their results allowed us to gain insight into how these different experiments can be used in applications to gather information concerning, for example, light with unknown wavelength, crystal lattices with unknown structures, or substances with unknown indices of refraction.

4 Acknowledgments

We would like to acknowledge Dr. Seog Oh and Yuriy Bomze for their mentorship and support during this project.

References

[1] Thompson, B.J. & Kingslake, R. Optics. Encyclopedia Britannica Online (2016). https://www.britannica.com/science/optics.

[2] Nave, C. R. Electromagnetic Spectrum. Hyperphysics (2012). http://hyperphysics.phy-astr.gsu.edu/hbase/ems2.html.

[3] Lucas, J. What Are Microwaves ? Live Science. LiveScience (2015). http://www.livescience.com/50259-microwaves.html.

[4] PASCO Scientific. Complete Microwave Optics System Experiment Guide WA-9316A. http://dcfa.exa.unicen.edu.ar/lab/manuales/cubo_de_bragg.pdf.

[5] Nave, C. R. Reflection and Fermats Principle. Hyperphysics (2012). http://hyperphysics.phy-astr.gsu.edu/hbase/phyopt/fermat.html.

[6] Fermat's Principle and the Laws of Reflection and Refraction. UCSC. Pearson Education (2008). http://scipp.ucsc.edu/~haber/ph5B/fermat09.pdf

[7] Nave, C. R. Fermat's Principle and Refraction. Hyperphysics (2012). http://hyperphysics.phy-astr.gsu.edu/hbase/phyopt/fermat.html#c3

[8] Fermat's Principle and the Laws of Reflection and Refraction. UCSC. Pearson Education (2008). http://scipp.ucsc.edu/~haber/ph5B/fermat09.pdf

[9] Polyanskiy, Mikhail. Refractive index database. Refractiveindex.info (2008). http://refractiveindex.info/?shelf=other&book=air&page=Ciddor

[10] Paraffin wax. Museum of Fine Arts Boston: Materials Database (2016). http://cameo.mfa.org/wiki/Paraffin_wax

[11] Nave, C. R. Crossed polarizers. Hyperphysics (2012). http://hyperphysics.phy-astr.gsu.edu/hbase/phyopt/polcross.html

[12] Nave, C. R. Bragg's Law. Hyperphysics (2012). http://hyperphysics.phy-astr.gsu.edu/hbase/quantum/bragg.html

[13] D.D. Johnson. MSE 280: Introduction to Engineering Materials, Chapter 3 (2004). MSE at Illinois. https://nanohub.org/resources/5488/download/ch3_p3.pdf

[14] Boundless. Huygens' Principle. Boundless Physics. Boundless, 01 Jun. 2016. h ttps://www.boundless.com/physics/textbooks/boundless-physics-textbook/wave-optics-26/ diffraction-175/huygens-principle-636-5593/

[15] Parry Hill, Matthew J. & Davidson, Michael W. Thomas Young's Double Slit Experiment (2015). Florida State University. http://micro.magnet.fsu.edu/primer/java/interference/doubleslit/